Environmental Science Nano

PAPER

View Article Online
View Journal | View Issue

Cite this: *Environ. Sci.: Nano*, 2016, 3, 768

Effects of low-molecular-weight organic acids on the dissolution of hydroxyapatite nanoparticles†

Dengjun Wang,[a] Yunsong Xie,[b] Deb P. Jaisi*[a] and Yan Jin*[a]

Received 26th March 2016,
Accepted 14th May 2016

DOI: 10.1039/c6en00085a

rsc.li/es-nano

Hydroxyapatite nanoparticles (HANPs) have recently been advocated as a highly efficient and environmentally benign 'green' phosphorus (P) nanofertilizer in modern agriculture. However, knowledge of how low-molecular-weight organic acids (LMWOAs) secreted by plants in agricultural soils mediate the dissolution of HANPs and release of dissolved phosphate is nonexistent. Here, three of the most commonly occurring LMWOAs (acetic, oxalic, and citric acids) were evaluated for their roles in HANPs dissolution in both batch and column systems. Particularly, O-isotopic ratios of dissolved phosphate during HANPs dissolution were measured to disentangle mechanisms controlling isotope fractionation. Our results reveal that in a batch system HANPs dissolution was very fast but the overall dissolution efficiency was low (≤30%), unlike in a column system where ~100% dissolution was achieved. The low dissolution efficiency of HANPs in the batch system was due predominantly to rapid consumption of protons, whereas in the column system the HANPs were progressively dissolved by low pH LMWOAs and reaction products were eluted out. Regardless of LMWOA type and experimental system, the isotopically lighter phosphate ($P^{16}O_4$) was preferentially released during the initial phases of dissolution and dissolved phosphate became gradually $P^{18}O_4$-enriched with time. This fractionation was less in batch (−0.3‰ to +1.1‰) than in column (−1.3‰ to +1.1‰) systems due primarily to lower dissolution efficiency and higher $P^{16}O_4$ and $P^{18}O_4$ exchange between HANPs and dissolved phosphates. The Rayleigh model well described O-isotopic fractionation of dissolved phosphate under different LMWOAs. Overall, our findings provide important insights into the dissolution kinetics and O-isotopic evolution of phosphate-based NPs that are relevant to plant–soil systems particularly at the rhizosphere.

Nano impact

The roles of naturally occurring low-molecular-weight organic acids (LMWOAs) in the dissolution of hydroxyapatite nanoparticles (HANPs) were explored. Our results indicate that phosphate release during HANPs dissolution is highly dependent on the type of LMWOA, which has important implications when HANPs are used as a promising phosphorus (P) nanofertilizer in agricultural soils particularly at the rhizosphere. Furthermore, a stable oxygen isotope technique was employed for the first time to accurately trace O-isotopic fractionation and evolution of phosphate during HANPs dissolution in abiotic systems. Given that the HANPs pool has distinct phosphate oxygen isotope signatures compared to soil P pools, the isotope technique could be used to identify whether plant uptake of P comes from HANPs or from soils and thus to evaluate the use efficiency of HANPs by plants in agricultural soils.

1. Introduction

Nanotechnology has been increasingly used as a powerful tool to augment plant nutrient uptake, maximize crop productivity, and improve food quality and thus the sustainability of modern agriculture.[1,2] Apatite is the primary phosphate mineral reserve on earth and has long been used for manufacturing phosphorus (P) fertilizers, but this reserve is diminishing rapidly.[3] Structurally, apatite has a hexagonal atomic framework, in which there is a dominant element (primarily Ca) on two of the cation sites and P on the third cation site (*e.g.*, calcium phosphate apatite). Another structural site of the calcium phosphate apatite can accommodate F, Cl, and OH, forming fluorapatite, chlorapatite, and hydroxyapatite, respectively.[4] Recent studies suggest that synthesized hydroxyapatite nanoparticles (HANPs; $Ca_5(PO_4)_3OH$) may be used as an efficient and environmentally friendly 'green' P nanofertilizer for crop production with reduced negative impacts, compared to commonly used commercial

[a] *Department of Plant and Soil Sciences, University of Delaware, Newark, DE 19716, USA. E-mail: jaisi@udel.edu, yjin@udel.edu; Fax: +1 302 831 0605; Tel: +1 302 831 1376, +1 302 831 6962*
[b] *Department of Physics and Astronomy, University of Delaware, Newark, DE 19716, USA*

† Electronic supplementary information (ESI) available: Includes Tables S1 and S2 and Fig. S1–S12. See DOI: 10.1039/c6en00085a

fertilizers, on water quality due to their nanoscale dimensions, large reactive surface area, and low leaching potential.[5,6] For example, Liu and Lal[5] showed that HANPs increased the growth rate and seed yield of soybeans cultivated in a greenhouse by 33% and 20%, respectively, compared to soybeans that received a regular P fertilizer ($Ca(H_2PO_4)_2$). Montalvo *et al.*,[6] however, reported that HANPs were more efficient than bulk-sized hydroxyapatite, but not as efficient as commercial fertilizers in wheat uptake of P in Andisols and Oxisols rich in iron and aluminum oxides. Clearly, research on the evaluation of HANPs as a promising P nanofertilizer is in the very early stages of development, and systematic studies are needed on P release kinetics of HANPs to address questions of whether and how HANPs could surpass commercial fertilizers for steady supply of P to plants, and/or offer other environmental advantages such as limited P leaching and loss or conditioning soil pH.

Biogeochemical cycling including plant uptake of P in soils is initiated after dissolution of apatite,[7] such as HANPs when they are used as a promising P nanofertilizer. Dissolution of apatite in soils particularly in the rhizosphere is predominantly controlled by protons and low-molecular-weight organic acids (LMWOAs) that are released as organic matter decomposition products, microbial metabolites, or root exudates at concentrations ranging from micro- to millimolar.[8–10] The most frequently occurring mono-, di-, and tri-carboxylic LMWOAs in the rhizosphere are acetic, oxalic, and citric acid, respectively.[8–10] The proposed mechanisms of apatite dissolution by LMWOAs include (1) proton-promoted dissolution (LMWOA elevates proton concentration); (2) ligand-controlled dissolution (LMWOA complexes with apatite and then breaks the metal–oxygen bond); and (3) formation of aqueous metal–ligand complexes that decrease the extent of relative saturation of metal (*e.g.*, Ca^{2+}) in solution.[11–13] Understanding the kinetics and mechanisms of HANPs dissolution by LMWOAs will provide necessary information for identifying effective approaches for improving HANPs' use efficiency and crop productivity simultaneously in agricultural soils.

Oxygen isotope ratios of phosphate in apatite mineral and dissolved phosphate ($\delta^{18}O_P$) have been increasingly applied as a powerful environmental geochemical indicator to gain better knowledge of environmental/temperature conditions under which apatite minerals (*e.g.*, tooth enamel, bones, and fish remains) are formed[14–16] and for tracing sources and understanding the biogeochemical cycling of P in natural environments.[17–20] This is because phosphate is primarily cycled in biological systems where rapid O-isotope exchange occurs between phosphate and ambient water *via* enzyme-catalyzed reactions, which may lead to complete isotope exchange.[17,21] In contrast, in abiotic systems, O-isotope exchange between phosphate and water is negligible at low temperature (<80 °C) and near-neutral pH conditions.[22,23] To expand the application of $\delta^{18}O_P$ values as an indicator of mineral dissolution and P uptake by plants, additional understanding of the physicochemical and biological processes and reactions leading to potential isotope fractionation is required.[24] To date, although several aspects of O-isotopic systematics involving microbial metabolism in biological systems[17,18] and abiotic interactions such as phosphate sorption,[25] desorption,[25] transport,[26,27] and mineral precipitation[28] and transformation[25,29] have been characterized in limited systems and environments, research dedicated to isotope effects associated with apatite dissolution is rare.[28] Particularly, O-isotopic fractionation during apatite dissolution by LMWOAs in plant–soil systems has not been explored.[30]

Our objectives were to (1) unravel the roles of LMWOAs (acetic, oxalic, and citric acids) in the dissolution of HANPs in both batch and column systems and (2) decipher the mechanisms of O-isotopic fractionation and isotope evolution during HANPs dissolution by LMWOAs in abiotic systems. Our results provide insights into the dissolution kinetics of phosphate-based NPs and expand the phosphate oxygen isotope systematics to differentiate reactions during apatite dissolution and isotope exchange when the dissolution is initiated.

2. Materials and methods

2.1. HANPs and LMWOAs

HANPs were purchased from Nanjing Emperor Nanomaterial Co. Ltd., China. The physicochemical properties of HANPs have been well characterized previously.[31,32] Briefly, HANPs are single-phase pure hydroxyapatite minerals and display a rod morphology with dimensions of 20 nm (width) by 100 nm (length). The Ca/P molar ratio of the HANPs is 1.65 and the specific surface area (SSA) is 154 $m^2\ g^{-1}$ (N_2-BET method). The three most commonly occurring LMWOAs, *i.e.*, acetic, oxalic, and citric acids, were chosen as model organic compounds, and an environmentally relevant concentration of 1 mM (ref. 8 and 9) was used.

2.2. Batch and column experiments

Laboratory-scale batch and column experimental systems under oxic condition and light were used to elucidate HANPs dissolution kinetics under different LMWOAs. Prior to use, batch and column experimental apparatuses (polypropylene tube and glass chromatography column) were soaked in 1 N HNO_3 overnight and then thoroughly cleaned with DI water. Batch experiments were performed in polypropylene tubes, where phosphate released during dissolution was monitored as a function of time. Briefly, 8 or 40 mg of HANPs powder was weighed into tubes containing 40 mL of DI water (control experiment) or 1 mM LMWOAs (acetic, oxalic, and citric acids), yielding 0.2 or 1 g L^{-1} HANPs. The high concentration (1 g L^{-1}) was included because it has been commonly used in mineral dissolution studies.[33] All batch experiments were conducted in triplicate and the tubes were shaken at 100 rpm for 120 h at 25 °C. The shaking speed was sufficient to keep the suspension well mixed but without causing turbulence that might cause abrasion of the HANPs.[33] At each sampling interval, a 2.5 mL aliquot was extracted from each tube and

immediately ultrafiltrated using a stirred ultrafiltration cell (Amicon Model 8010, Millipore Corp., Bedford, MA) with a 10 kDa cellulose membrane (PLGC02510) equivalent to nominal particle sizes of 5–6 nm (ref. 34) to separate dissolved phosphate. P species in the ultrafiltrate are assumed to be dissolved PO_4^{3-} ions because undissolved (or partially dissolved) HANPs cannot pass through the 10 kDa membrane.[32] The clear ultrafiltrate exhibited no detectable plasmon resonance optical absorption peak,[35] confirming the ability of ultrafiltration to remove undissolved HANPs.

Complementary to mechanistic examination of HANPs dissolution by LMWOAs in the batch system, additional sample characterizations were performed. The average hydrodynamic diameters (D_H) of HANPs under different LMWOAs *versus* time were analyzed using a dynamic light scattering method (DLS; Möbiuζ, Wyatt Technology Corp., Santa Barbara, CA). Furthermore, after completion of the batch experiments, some undissolved (or partially dissolved) HANPs were freeze-dried and analyzed using a transmission electron microscope (JEM 2010F TEM, JEOL, Japan) to investigate the morphological changes of HANPs after interacting with LMWOAs.

Particularly, column experiments were conducted to aid in better interpretation of kinetic data as in such experiments reaction products are continuously removed and therefore back reaction and reaction inhibition can be avoided.[33] Column experiments were conducted in duplicate using a sequential deposition–dissolution procedure. Briefly, a glass chromatography column (1.6 cm inner diameter × 9 cm long) was dry-packed with 31.5 g of quartz sand (688 μm in diameter) that was thoroughly cleaned previously (1 N HNO_3 and 1 N NaOH, respectively) to remove any adsorbed clays and/or metal oxide impurities,[32] yielding a bulk density of 1.74 g cm^{-3} and pore volume (PV) of 7.4 mL. Twenty PVs of DI water (pH 6.5) were subsequently injected in an upflow mode at an environmentally relevant flow rate (q) of 0.044 cm min^{-1} (ref. 36) to slowly saturate the column (retention time for tracer is 74 min). The gravimetrically measured porosity of the packed column was approximately 0.32. Following the saturation step, a deposition experiment was initiated by injecting 5 PVs of 0.2 g L^{-1} HANPs suspension (pH 6.5) into the column, followed by elution with 5 PVs of DI water (pH 6.5) at q = 0.044 cm min^{-1}. The 0.2 g L^{-1} HANPs concentration used in both batch and column deposition experiments was consistent with that in a HANPs transport study.[32] The deposition experiments mimic nanomaterials' accidental release and subsequent transport along the soil profile,[37] or intentional application of NPs (*e.g.*, NZVI) for environmental remediation.[38] After completion of the deposition experiment, the HANPs dissolution experiment was initiated by continuously injecting 20 PVs of 1 mM LMWOA (acetic, oxalic, or citric acid) at q = 0.044 cm min^{-1}. Our preliminary experiments revealed that 20 PVs of LMWOA were adequate to dissolve the HANPs retained in the column.

Column effluents were collected continuously using a fraction collector (Foxy Jr., Teledyne Isco, Lincoln, NE). The concentrations of dissolved phosphate in samples from batch and column experiments were measured on a spectrophotometer (Beckman DU 640, Beckman Instruments Inc., Fullerton, CA) using the phosphomolybdate blue colorimetric method,[39] whereas the concentrations of HANPs in column deposition experiments were determined spectrophotometrically at the wavelength of 300 nm.[40] The pH of HANPs suspensions and effluents in batch and column experiments was monitored using a pH meter (Accumet Excel XL50, Fisher Scientific). To fully understand the mechanisms of HANPs dissolution by LMWOAs, the chemical speciation of LMWOAs *versus* pH was calculated using the Visual MINTEQ 3.0 software.

2.3. Phosphate oxygen isotope ratio measurements

Ultrafiltrate and effluent samples from batch and column experiments (*i.e.*, dissolved phosphate) and selected solid-phase samples that were intercepted by the 10 kDa membrane (undissolved and/or partially dissolved HANPs) in batch experiments were individually processed for O-isotopic analyses. All samples were purified using sequential precipitation and recrystallization methods.[24] Briefly, each sample was first treated with Supelite DAX-8 resin (Supelco, Bellefonte, PA) to remove dissolved organic matter (*e.g.*, LMWOAs),[41] precipitated as ammonium phosphomolybdate (APM), and then recrystallized as magnesium ammonium phosphate (MAP), as described by Jaisi and Blake.[24] MAP was dissolved and the resulting solution was treated using AG X-8 cation resin (Bio-Rad) to remove Ca^{2+} and other cations. The purified phosphate solution was finally precipitated as silver phosphate (Ag_3PO_4).

The $\delta^{18}O_P$ values were measured by online high-temperature thermal decomposition of Ag_3PO_4 to CO gas at 1460 °C using a Thermo-Chemolysis Elemental Analyzer (TC/EA) coupled to a Delta V continuous flow isotope ratio monitoring mass spectrometer (IRMS; Thermo, Bremen, Germany) with an analytical precision of ≤0.3‰ at the Stable Isotope Facility at the University of Delaware. The $\delta^{18}O_P$ values were calibrated against two Ag_3PO_4 standards, YR-1aR-02 (−5.49‰) and YR-3.2 (+33.63‰). For each run, the oxygen yield from Ag_3PO_4 was calculated and those within ±10% of that of an internal laboratory Ag_3PO_4 standard (Fisher Scientific) were accepted for isotope analyses. All O-isotopic data are reported relative to the Vienna Standard Mean Ocean Water (VSMOW) standard in units of permil (‰).

2.4. Data analyses

The dissolution efficiency (%) of HANPs in the batch experiments was calculated based upon the concentration ratio between dissolved phosphate and total phosphate in the suspension.

The dissolution rate (R; mol m^{-2} s^{-1})[33,42,43] of HANPs in batch and column experiments was determined as follows:

$$R = \frac{\Delta M}{S_i t} \quad (1)$$

where ΔM is the mass consumption (mol) of HANPs from time 0 to t (s) and S_i is the initial surface area (m^2) of HANPs (*i.e.*, SSA × mass), consistent with the approach of Welch *et al.*,[33] Guidry and Mackenzie,[42] and Chairat *et al.*[43] For a specific C_0, S_i is a fixed value, *e.g.*, S_i = 1.23 and 6.16 m^2, respectively, at 0.2 and 1 g L^{-1} HANPs in the batch experiments. In this study, the average dissolution rate (R_{ave}; mol m^{-2} s^{-1}) is employed to quantify the capability of LMWOA in HANPs dissolution, which refers to R when the dissolution reaction reaches equilibrium (or steady state),[44] *e.g.*, ~1 h and 2.5 PV, respectively, for batch and column experiments (as shown below).

The two-site dissolution model[45–47] was applied to describe HANPs dissolution kinetics under different LMWOAs in the batch experiments. Site 1 predominates when dissolution occurs under unsaturated solutions, *e.g.*, during the initial phases of dissolution, whereas site 2 becomes active during later stages particularly when dissolution approaches equilibrium, *e.g.*, (partial) saturation solutions.

$$\frac{dC}{dt} = k_1(C_{s1} - C) + k_2(C_{s2} - C) \quad (2)$$

$$C[PO_4^{3-}]_t = C[PO_4^{3-}]_{max1} \times (1 - e^{-k_1 t}) + C[PO_4^{3-}]_{max2} \times (1 - e^{-k_2 t}) \quad (3)$$

where eqn (2) is the analytical rate expression and eqn (3) is its integrated form; C is the concentration (mM) of dissolved phosphate; C_{s1} and C_{s2} are the 'apparent solubilities' (mM)[46,47] of dissolved phosphate associated with sites 1 and 2, respectively; k_1 and k_2 are the dissolution rate constants (h^{-1}) on sites 1 and 2, respectively; and $C[PO_4^{3-}]_{max1}$ and $C[PO_4^{3-}]_{max2}$ are the concentrations (mM) of total dissolved phosphate for sites 1 and 2, respectively.

The Rayleigh model has been widely used to describe trends on isotope fractionation[48] and was used to quantify ^{18}O enrichment factor (ε_0; ‰) in dissolved phosphates:

$$\mathrm{Ln}\left[\frac{\delta^{18}O_P + 1000}{\delta^{18}O_{P0} + 1000}\right] = \frac{\varepsilon_0}{1000}\ln\left(\frac{C_t}{C_0}\right) \quad (4)$$

where $\delta^{18}O_{P0}$ and $\delta^{18}O_P$ are the phosphate oxygen isotope ratios of starting HANPs (t = 0) and dissolved phosphate at time t during dissolution, respectively; and C_0 and C_t are the corresponding concentrations of starting HANPs and dissolved phosphate, respectively.

One-way ANOVA analysis was conducted to identify statistically significant differences among measured $\delta^{18}O_P$ values using Tukey's Honestly Significant Difference (HSD) test. The statistical analyses were performed using SPSS 16.0 software, and the differences of means were considered significant at $p < 0.05$.

3. Results and discussion

3.1. Dissolution of HANPs in batch experiments

Dissolution of HANPs in terms of efficiency and rate at initial HANPs concentrations (C_0) of 0.2 and 1 g L^{-1} under three LMWOAs (1 mM acetic, oxalic, and citric acid) in the batch system is shown in Fig. 1. A very rapid release of dissolved phosphate occurred initially (~0.2 h; Fig. 1a and c), and the release of dissolved phosphate then either remained constant or, in some cases, decreased slightly with time (C_0 = 1 g L^{-1}) until a steady state was reached. The dissolution efficiency followed the order acetic < oxalic < citric acid and was much higher at lower C_0 (0.2 g L^{-1}). These results were supported by the fact that the R value varied in the same order, acetic < oxalic < citric acid, and was larger at lower C_0 (Fig. 1b and d). Similar findings were observed on the dissolution of apatite minerals by inorganic[33,42] and organic acids (*e.g.*, LMWOAs).[33,49] This is due primarily to proton-promoted (mechanism 1) and ligand-controlled dissolution (mechanism 2; as shown in the ESI,† Fig. S1) and approaching solution saturation with respect to the dissolving species and/or possible secondary mineral phases in the batch system, which are discussed below in detail.

3.1.1. Proton-promoted dissolution. The dissolution rate of minerals such as oxides, silicates, and phosphates is proportional to the proton concentration, as has been shown in surface speciation modeling and surface titration experiments.[11] Kpomblekou and Tabatabai[49] further demonstrated that the amount of P released from phosphate rocks under different LMWOAs was significantly negatively correlated with solution pH. In our study, the initial pH of 1 mM LMWOAs (4.79, 3.90, and 3.60 for acetic, oxalic, and citric acids, respectively, at t = 0; Fig. 2a and b) and equilibrium pH of HANP–LMWOA suspensions (*e.g.*, 5.95, 5.17, and 5.03, respectively, at t = 120 min and C_0 = 0.2 g L^{-1}; Fig. 2a) followed the same order: acetic > oxalic > citric acid. Interestingly, there was an early fast increment in pH, followed by a much longer slow increase towards a nearly neutral pH during HANPs dissolution (Fig. 2a and b). This increase in pH was more pronounced at higher C_0 due primarily to faster and greater proton depletion in the suspension (ΔpH = 0.27–1.44 *vs.* 1.37–2.58 at C_0 = 0.2 and 1 g L^{-1}, respectively; Fig. 2c and d). Careful examination of the relationship between R and ΔpH revealed that the value of R decreased linearly with ΔpH, suggesting that the contribution of protons to HANPs dissolution became weaker during later stages (*i.e.*, larger ΔpH). Furthermore, the linear slope varied in the order of acetic > oxalic > citric acid, meaning that protons played a less important role in HANPs dissolution in acetic compared to oxalic and citric acids, consistent with the kinetic results (as shown in Fig. 1). Additionally, the linear slope was greater at higher C_0 (*e.g.*, −7 < −3 for acetic acid at C_0 = 0.2 and 1 g L^{-1}, respectively), indicative of less contribution of protons at higher C_0. Similar pH change phenomena were frequently reported on apatite mineral dissolution under acidic pH conditions where mineral-bound cations (*e.g.*, Ca^{2+}) are

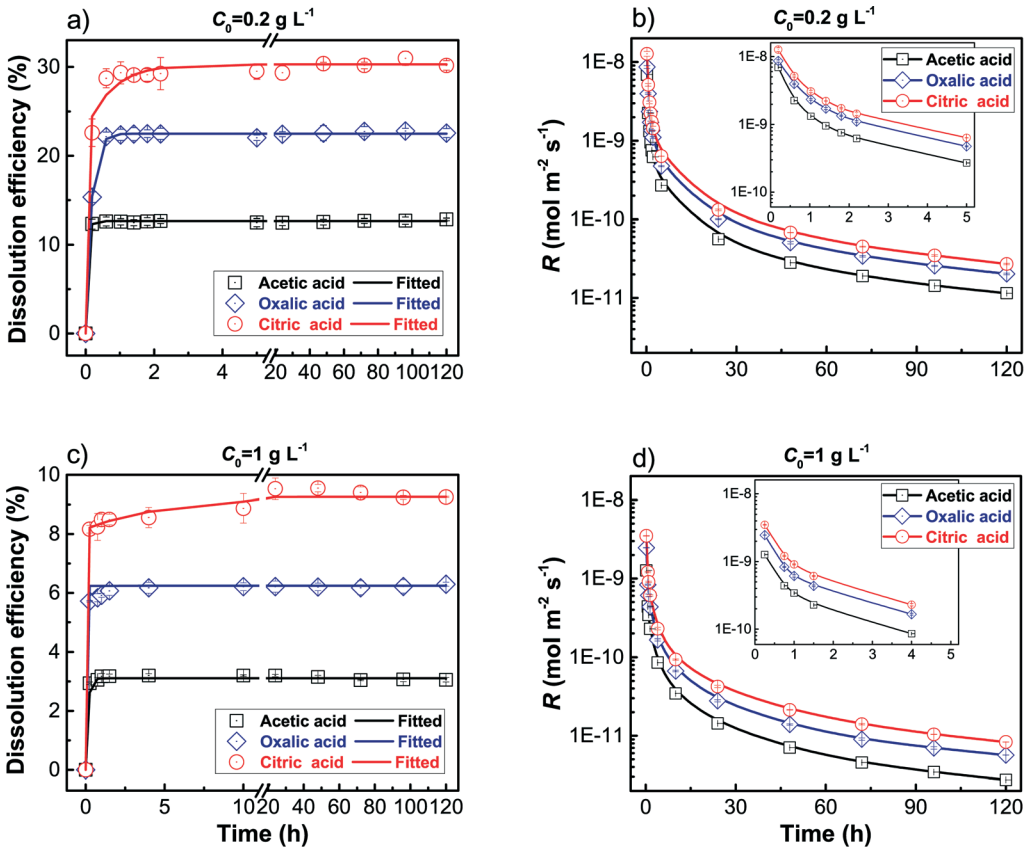

Fig. 1 Dissolution efficiency (%) and dissolution rate (R; mol m^{-2} s^{-1}) of HANPs as a function of time under different LMWOAs (1 mM acetic acid, oxalic acid, and citric acid, respectively) in batch experiments at initial HANPs concentrations (C_0) of 0.2 g L^{-1} (a and b) and 1 g L^{-1} (c and d), respectively. Error bars represent the standard deviations in triplicate experiments. Insets in (b) and (d) highlight R change during the early stages where y-axes are shown in logarithmic scale.

exchanged with protons at mineral surfaces and then released to the bulk solution, yielding a concomitant increase in solution cation concentrations and pH.[42] The chemical speciation of acetic, oxalic, and citric acids *versus* pH is included in the ESI† Fig. S2, which shows that proton dominates initially (t = 0, pH 3.60–4.79), but its concentration decreases progressively with pH (from 3.60 to 6.54) due to increased proton–cation exchange. The equilibrium pH of HANP–LMWOA suspensions remained in the range of 5.0–6.5 (Fig. 2a and b), which is commonly observed in apatite mineral dissolution.[33,42,50] Wu *et al.*[51] indicated that apatite has two surface groups, ≡P–O$^-$ and ≡CaOH$_2^+$, and that the ≡P–O$^-$ group protonates within pH 5–7 to form ≡P–OH^0 and the CaOH$_2^+$ group deprotonates within pH 8–10 to form ≡CaOH^0. Consequently, within pH 5.0–6.5, the ≡P–O$^-$ group controls the dissolution rate of HANPs.

3.1.2. Ligand-controlled dissolution. While distinguishing proton- and ligand-promoted effects is not straightforward in mineral dissolution experiments where pH is not held constant by buffering agents, we did not buffer the pH of HANPs suspensions because buffering agents can affect dissolution and result in high element background levels, thereby causing large errors after blank correction.[52–54] It is well known that organic ligands can promote mineral dissolution irrespective of pH buffering.[11–13,33,42] Here, organic ligands are expected to affect HANPs dissolution both directly and indirectly. First, organic ligands directly complex with metal ions (*e.g.*, Ca^{2+}) and weaken metal–oxygen bonds on mineral surfaces, thus catalyzing the release of metal to the solution. Equally importantly, organic ligands indirectly enhance mineral dissolution by complexing with metal ions already released to the solution, thus decreasing the effective concentration of metals in solution for preventing saturation. Additionally, organic acids buffer solution pH because dissociated protons are consumed during dissolution. The 'direct' and 'indirect' dissolution of HANPs by organic ligands occurs at the apatite crystal surface and in the bulk solution, respectively.[45] Regardless of C_0, acetic acid had the least effect compared to oxalic and citric acids on HANPs dissolution (Fig. 1). This is because organic ligands containing two or more donor atoms in functional (carboxyl) groups and capable of forming bi- or multi-dentate mononuclear surface chelates (oxalic and citric acids) that readily transfer electron density to the centers of the surface metal can accelerate the cleavage of metal–oxygen bonds and their eventual detachment from mineral surfaces.[11,12] Given that citric acid is subjected to different degrees of protonation depending on pH (Fig. S2†), it is important to explore the role of citrate ligands on HANPs

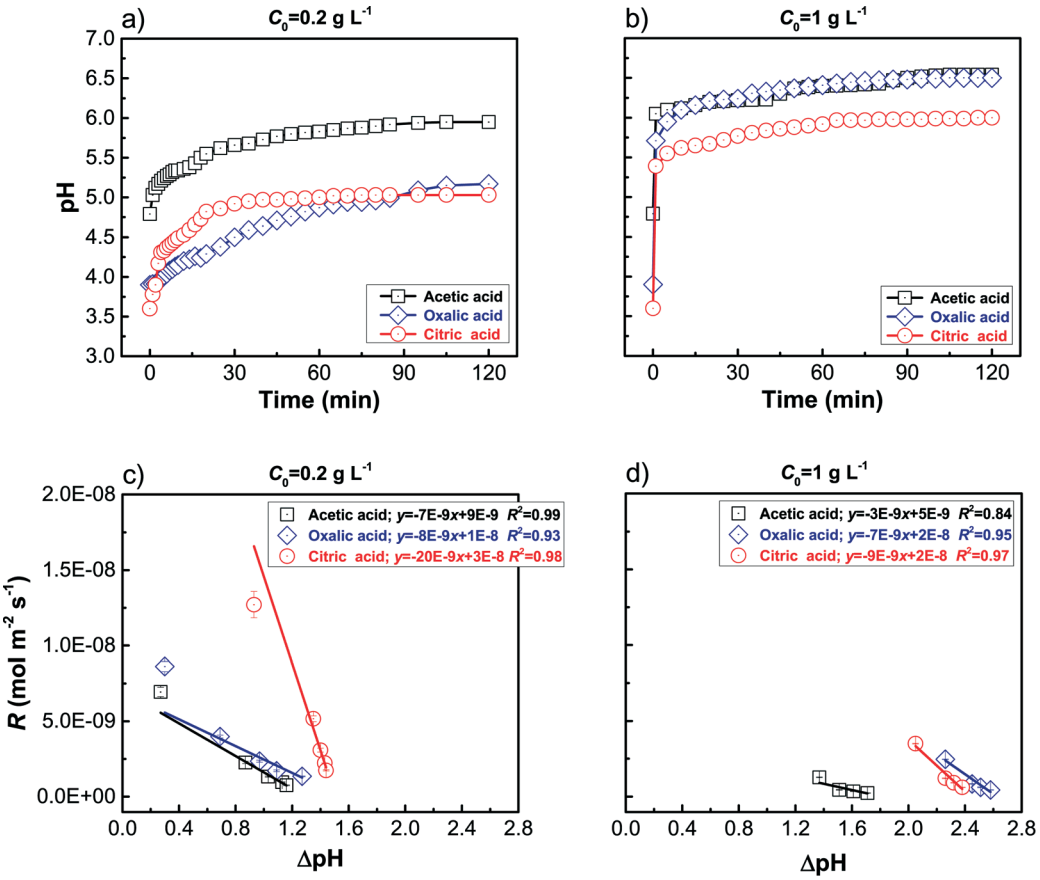

Fig. 2 Change in pH of HANPs suspension as a function of time (a and b) and relationship between pH change (ΔpH) and dissolution rate (c and d) under different LMWOAs (1 mM acetic acid, oxalic acid, and citric acid, respectively) in batch experiments at C_0 = 0.2 g L^{-1} (a and c) and 1 g L^{-1} (b and d), respectively. Error bars represent the standard deviations in triplicate experiments.

dissolution over the pH range encountered (pH 3.6–6.0; Fig. 2b). At pH 3.6, H_2-citrate$^-$ dominates with small amounts of H_3-citrate and H-citrate^{2-} ligands, whereas H-citrate^{2-} predominates when pH is elevated to 6.0. Based on computer simulations,[55] these citrate ligands are expected to thermodynamically coordinate with Ca^{2+} on HANPs surfaces through surface complexation reactions, forming Ca–H_2-citrate$^+$ and Ca–H-citrate complexes. However, at the onset of dissolution where proton concentration is high, proton exchanges with Ca^{2+} are much faster and more profound than that of ligand–Ca^{2+},[53] resulting in a rapid increment in pH during the early stages (Fig. 2a and b). The ligand–Ca^{2+} interaction does not become significant until the solution pH is high. Therefore, the Ca–H-citrate complex is likely to take over the dissolution during later stages where pH change is much smoother (Fig. 2a and b).

3.1.3. Dissolution rate (R) in batch experiments. Because proton and ligand determine HANPs dissolution at different stages, an exponential decay model that includes two different decay coefficients (d_1 and d_2) was employed to quantify the contribution of protons (d_1) and ligand (d_2) in R change *versus* time in the batch experiments (ESI,† Fig. S3 and Table S1). The selection of the two-decay-coefficient model is also supported by the findings of R_{net} *vs.* Δt (where R_{net} characterizes the net dissolution rate over a specified time interval; as shown in the ESI,† Fig. S4) that R_{net} decreased significantly initially but remained relatively constant during later stages; thus a one-decay-coefficient model cannot accurately capture these features (Fig. S3 and S4†). Our modeling results clearly indicate that the contribution of protons is much greater than that of ligand because $d_1 \gg d_2$ (Table S1†). Moreover, both values of d_1 and d_2 varied in the same order, acetic < oxalic < citric acid, implying the greater contribution of citric than acetic and oxalic acids. These findings are important for selecting appropriate models to capture HANPs dissolution kinetics under different LMWOAs in the batch experiments (Fig. 1), as described below.

In a batch system, solution saturation impacts mineral dissolution rate.[33,42] For undersaturated conditions, the activity of a chemical species between solid and solution decreases when its concentration in solution elevates, resulting in a reduction in dissolution rate as the solution approaches saturation (*e.g.*, PO_4^{3-} ion; Fig. 1). On the other hand, removal of ions due to precipitation has an opposite effect. For example, oxalic acid can precipitate as Ca-oxalate, which promotes HANPs dissolution by lowering Ca^{2+} concentration in the solution.[33,53]

We additionally analyzed the relationships between average dissolution rate (R_{ave}) and the number of carboxyl groups (N) and R_{ave} and consumed amount of protons when the dissolution reaction reaches equilibrium, respectively at C_0 = 0.2 and 1 g L^{-1} in the batch experiments (ESI,† Fig. S5). The value of R_{ave} increased linearly with N (Fig. S5a†), confirming that the carboxyl group affects the dissolution rate of HANPs. The R_{ave} values were much smaller at C_0 = 1 g L^{-1} than at C_0 = 0.2 g L^{-1} due primarily to more rapid depletion of protons. In addition, the R_{ave} value was observed to increase linearly with consumed amount of protons and the slope was higher at lower C_0 (Fig. S5b†), consistent with the correlation between R and ΔpH (Fig. 2c and d). These results clearly verify that the amount of protons controls HANPs dissolution and the effect is more pronounced at lower C_0 in the batch experiments. The R_{ave} values obtained in our study, *i.e.*, $(2.3 \pm 0.005) \times 10^{-10}$ to $(3.1 \pm 0.1) \times 10^{-9}$ mol m^{-2} s^{-1}, are consistent with those in published literature on apatite minerals,[33,42,50] because R is normalized by the initial surface area of apatite. For example, within pH 2.2–6.7, Valsami-Jones *et al.*[50] found that R ranged from 1.8×10^{-9} to 3.0×10^{-9} mol m^{-2} s^{-1} for natural apatite and from 4.5×10^{-11} to 2.3×10^{-9} mol m^{-2} s^{-1} for synthetic apatite. Welch *et al.*[33] observed that R increased from 2×10^{-10} to 2×10^{-9} mol m^{-2} s^{-1} for natural apatite when pH was decreased from 5.5 to 4.0. The small discrepancy in R between our and past studies could be due to a number of factors including differences in experimental procedures (solution type, volume, and saturation state, and shaking rate) and properties of apatite mineral (size, surface roughness, and surface area), which altogether influence apatite solubility and reactivity.

To better discern the contribution of proton and ligand to HANPs dissolution in the batch experiments, the linear slopes of *R vs.* ΔpH and *R vs. N* are compared (Fig. 2 and S5a†). Our results show that the linear slope of *R vs. N* was steeper at lower C_0 (Fig. S5a†), indicative of greater contribution of ligand at lower C_0, recalling that protons also play more pronounced roles at lower C_0, both of which contribute to the greater dissolution of HANPs at lower C_0 (Fig. 1). Most notably, the linear slope (absolute value) of *R vs.* ΔpH was 1–2 orders of magnitude greater than that of *R vs. N* (note that the slope of *R vs.* consumed amount of protons is a different story because the values of consumed proton amount are not on the same magnitude as those of ΔpH and N, as shown in Fig. 2 and S5†), demonstrating the dominant role of protons in HANPs dissolution in batch experiments, which is in agreement with the results obtained from the two-decay-coefficient model (Fig. S3 and Table S1†). These findings are expected because >90% HANPs dissolution was completed during early stages (*e.g.*, 0.2 h; Fig. 1) where proton concentration is high.

3.1.4. Dissolution rate constant (k) in batch experiments. The two-site dissolution model well captured HANPs dissolution kinetics under three LMWOAs in the batch experiments ($R^2 \geq 0.99$; Fig. 1 and ESI† Table S2). The values of both $C[PO_4^{3-}]_{max1}$ and k_1 on site 1 were higher than those of site 2 $C[PO_4^{3-}]_{max2}$ and k_2 (with the exception of k_2 in acetic acid), meaning that site 1 controls the overall dissolution of HANPs particularly during early phases (Fig. 1a and c), and dissolution on site 2 becomes active only during later stages where the solution approaches (partial) saturation, thereby resulting in a decrease in R (Fig. 1b and d). These findings quite agree with the respective contribution of proton and ligand on HANPs dissolution (described above). Both values of $C[PO_4^{3-}]_{max}$ and k on either site were higher at lower C_0, implying that HANPs dissolution was faster at lower C_0. Most importantly, the k_1 values generally followed the order $k_{1\text{-acetate}} < k_{1\text{-oxalate}} < k_{1\text{-citrate}}$, substantiating that HANPs dissolution was the lowest for acetic and the highest for citric acid, analogous to their carboxyl group contents (Fig. S5a†). In contrast, the k_2 values exhibited an inconsistent behavior likely because back reaction and reaction inhibition occurred when dissolution approached equilibrium,[45] thereby obscuring the trends of k_2 at varying LMWOAs. It is noteworthy to mention that the k values obtained for the HANPs are ≥1 order of magnitude greater than those for bulk apatite minerals.[33,42,50,53,56] This is because HANPs dissolution is size dependent and the HANPs in our study are smaller (≤100 nm) and have higher SSA (154 m^2 g^{-1}) compared to those in the literature (20–1000 μm and 0.026–16 m^2 g^{-1}, respectively, for bulk apatite minerals),[33,42,50,53,56] *i.e.*, the smaller size and higher SSA, the larger the k.[57,58]

Previous studies demonstrate a linear dependence between dissolution rate and rate constant on HANPs dissolution under acidic pH conditions.[42,43] A similar linear relationship was obtained between R_{ave} and k_1 (reflects the contribution of proton) under different C_0 and LMWOAs in the batch experiments (ESI† Fig. S6). These findings again substantiate the predominance of protons in HANPs dissolution in the batch experiments. Please note that although citric acid has an additional OH^- group, which would affect the dissolution of HANPs, the contribution of the OH^- group to HANPs dissolution is expected to be negligible because (1) protons control the overall dissolution of HANPs (described above), and (2) the OH^- group plays a less important role in HANPs dissolution compared to that of the $COOH^-$ group.

Monitoring the changes in size and morphology of HANPs during dissolution by LMWOAs shows that the D_H value of HANPs decreased drastically during early phases of dissolution (0–10 min) and then remained constant throughout steady-state conditions (ESI† Fig. S7), consistent with the trends of HANPs dissolution kinetics (Fig. 1). The D_H value of HANPs was in the order acetic > oxalic > citric acid, again confirming the greater role of citric acid in accelerating HANPs dissolution than that of oxalic and acetic acids. The TEM images show that the pristine HANPs are rod-shaped, measuring 20 nm wide and 100 nm long (ESI† Fig. S8a). In LMWOA solution, etching of HANPs led to the formation of different shaped HANPs (spherical, ellipsoidal, diamond, and triangular; Fig. S8b–d†) because etching is not likely to be controlled by crystal defect-induced dissolution on HANPs surfaces due to large SSA and high surface free energy. This information could be helpful for synthesizing apatite-type

nanofertilizers having different shapes because the efficiency of a nanofertilizer in soils (porous medium) is dependent on its mobility, which is related to particle shape.[59,60] It should be mentioned that in this study, R (and R_{ave}) is normalized to the initial surface area of HANPs (eqn (1)), which is a fixed value at a given C_0. Nonetheless, the size and shape of HANPs were observed to be altered during dissolution (Fig. S7 and S8†), which would affect R. Because the dissolution efficiency of HANPs varied in the order of acetic < oxalic < citric acid and was lower at higher C_0 (Fig. 1a and b), the actual surface area of HANPs during dissolution is expected to follow the trend of acetic > oxalic > citric acid and is greater at higher C_0. Consequently, the actual value of R (and R_{ave}) would follow the same trend of acetic < oxalic < citric acid (*i.e.*, the same as that obtained by normalizing the initial surface area of HANPs) and be much larger for citric than oxalic and acetic acids particularly at lower C_0.

3.2. Dissolution of HANPs in column experiments

The breakthrough curve and retention profile of HANPs at C_0 = 0.2 g L^{-1} in the column deposition experiment are presented in the ESI† Fig. S9, which show that the mobility of HANPs was rather limited (~5% broke through) and most of the HANPs were retained (~7.03 mg of HANPs) particularly near the column inlet (0–3 cm), consistent with our previous results.[31,32] These phenomena are largely due to aggregation and straining of HANPs in a porous medium. No wall effect and preferential flow occurred in the transport experiments because of the symmetrical breakthrough curve of the tracer (ESI† Fig. S10).

The effect of LMWOA type on the dissolution of HANPs (C_0 = 0.2 g L^{-1}) in the column system is shown in Fig. 3. An initial peak of dissolved phosphate occurred after the onset of HANPs dissolution, which was the lowest for acetic and the highest for citric acid. The higher peak of dissolved phosphate in citric than oxalic and acetic acids is consistent with the greater capability of citric acid, allowing faster dissolution of HANPs (as observed in the batch system). In contrast, the duration of the phosphate peak varied in the order of acetic > oxalic > citric acid (Fig. 3a), *i.e.*, the peak plateau maintained ~6, 3, and 1 PV, respectively, in acetic, oxalic, and citric acid. To demonstrate more explicitly that the plateau of phosphate release is a general phenomenon in column dissolution experiments, a 5-fold higher loading of HANPs (5 PVs of 1 g L^{-1} HANPs suspensions) was used in the column deposition experiment. A much longer duration (~35 PVs) and lower peak

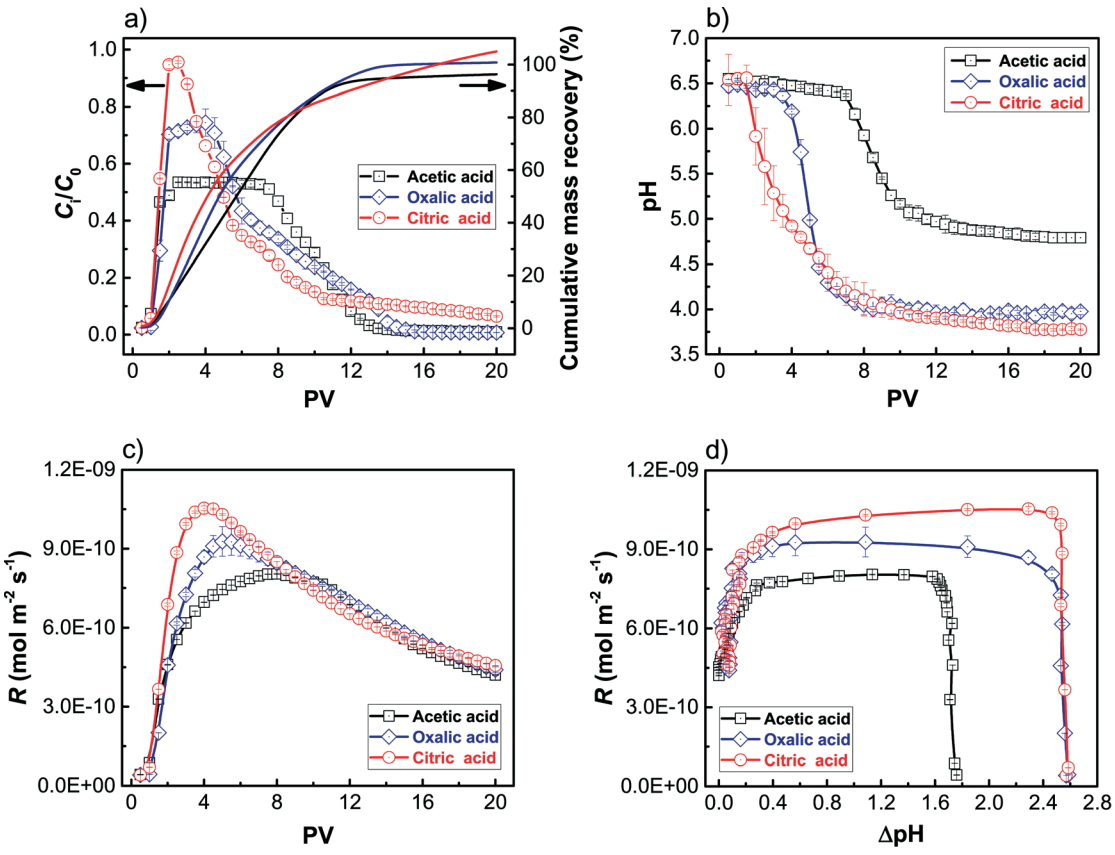

Fig. 3 Normalized effluent concentration (a; left y-axis), cumulative effluent mass recovery (a; right y-axis), effluent pH (b), and dissolution rate (c) as a function of PV, and relationship between pH change and dissolution rate (d) when continuously injecting 20 PVs of 1 mM LMWOAs (acetic acid, oxalic acid, and citric acid, respectively) to dissolve the HANPs retained in the column at C_0 = 0.2 g L^{-1}. Error bars represent the standard deviations.

value (C_i/C_0 = 0.007) of dissolved phosphate were obtained (ESI† Fig. S11a) compared to those at a lower HANPs loading (Fig. 3a). These observations are anticipated because HANPs dissolution in a dynamic column system removes dissolved phosphate and maintains undersaturated conditions,[44] yielding a ~100% dissolution (96.3–105%; Fig. 3a) of HANPs, and the lower peak value observed at a higher HANPs loading in the column system reflects a slower dissolution rate, with the order consistent with that of the batch system. The trend of pH change upon the injection of LMWOAs (Fig. 3b and S11b†) is in excellent agreement with that of HANPs dissolution kinetics (Fig. 3a and S11a†), indicative of the predominance of proton in HANPs dissolution in the column system. Release of phosphate decreased progressively and tended to approach zero. Such a gradual decrease in phosphate release is frequently encountered in flow-through column experiments[44] and has been attributed to the reduced HANPs that are available for dissolution. At the end of the column dissolution experiments, effluent pH became close to the initial pH of 1 mM LMWOAs (Fig. 3b). Interestingly, at the end of the column experiments, pH in the effluent was 1.7–2.4 pH units lower than the equilibrium pH of HANP–LMWOA suspension in batch experiments (Fig. 2b), again substantiating that pH is the key factor controlling the rate and extent of HANPs dissolution.

3.2.1. Dissolution rate (R) in column experiments. In line with the findings obtained in the batch experiments (Fig. 1b and d), the peak value of R varied in the same order: acetic < oxalic < citric acid (Fig. 3c). However, the overall trend of R *vs.* PV (*i.e.*, time) in column experiments was distinct from that in batch experiments. Specifically, R increased and soon achieved the maximum at the end of the peak plateau (Fig. 3a and c) and then decreased progressively during later stages due to fewer HANPs in the column available for dissolution (described above). Regardless of LMWOA type, R tended to approximate the same value at the end of dissolution because ~100% HANPs were dissolved. With increasing ΔpH, R increased and reached the peak plateau in column experiments (Fig. 3d), consistent with the observations of R *vs.* PV. Again, R decreased during later stages (larger ΔpH) due to the limited HANPs in the column system. It should be mentioned that in the 'open' column system where low pH LMWOA is continuously injected, the dissolution rate of HANPs is dependent on the transient pH of pore-water and the amount of HANPs available for dissolution, and ligands are expected to play much less of a role compared to those in the 'closed' batch system. The R_{ave} value in column experiments followed the same order: acetic < oxalic < citric acid. The column system produced R_{ave} values ranging from (5.6 ± 0.003) to (8.9 ± 0.06) × 10^{-10} mol m^{-2} s^{-1}, consistent with those ((2.3 ± 0.005) × 10^{-10} to (3.1 ± 0.1) × 10^{-9} mol m^{-2} s^{-1}) in the batch system. These findings demonstrate that R is inherently compound (LMWOA type) dependent rather than system (batch/column) dependent.

3.3. Phosphate oxygen isotope fractionation during HANPs dissolution

To decipher the mechanisms controlling phosphate oxygen isotope fractionation and isotope evolution over time during HANPs dissolution by LMWOAs, $\delta^{18}O_P$ values of dissolved phosphate and undissolved HANPs were measured. The $\Delta^{18}O_P$ values (*i.e.*, difference in isotope values between dissolved phosphate and bulk (starting) HANPs) under three LMWOAs in both batch and column experiments are presented in Fig. 4, which shows that the $\Delta^{18}O_P$ was negative at first and then increased unidirectionally towards a positive value over the course of dissolution. Conversely, the $\Delta^{18}O_P$ values between undissolved and bulk HANPs in 1 mM oxalic acid in batch experiments (ESI† Fig. S12) show that its $\Delta^{18}O_P$ was positive initially and decreased gradually with phosphate release. These observations suggest that the lighter isotopes in the P–O bond ($P^{16}O_4$) are preferentially broken and released to the solution during early stages of dissolution, resulting in products (dissolved phosphate) with lighter

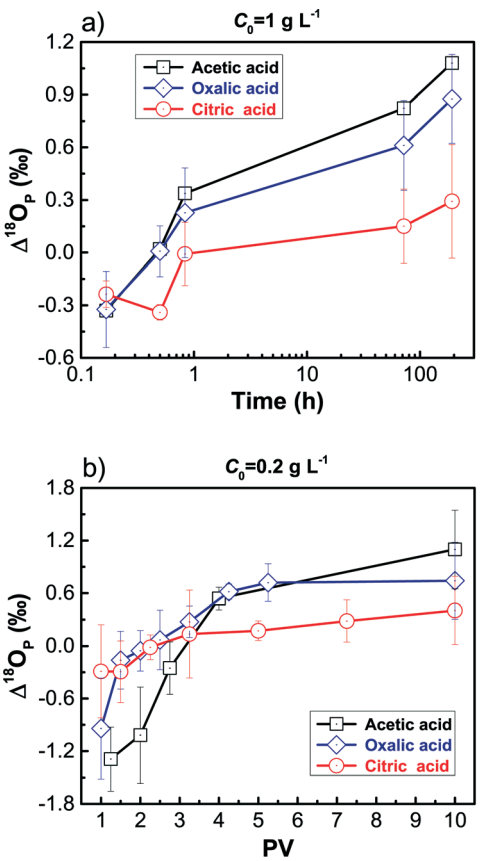

Fig. 4 Phosphate oxygen isotope ratios of dissolved phosphate in batch (a; C_0 = 1 g L^{-1}) and column (b; C_0 = 0.2 g L^{-1}) dissolution experiments as a function of time under different LMWOAs (1 mM acetic acid, oxalic acid, and citric acid, respectively). Standard deviation is calculated from the isotopic composition of phosphate from each sample. The $\Delta^{18}O_P$ describes phosphate oxygen isotope fractionation of dissolved phosphate ($\delta^{18}O_P$) relative to the bulk (starting) HANPs ($\delta^{18}O_{P0}$), *i.e.*, $\Delta^{18}O_P = \delta^{18}O_P - \delta^{18}O_{P0}$.

isotopes, which is a common feature for oxygen isotope fractionation of oxyanions, *e.g.*, nitrate,[61] carbonate,[62] and sulfate,[63] in biogeochemical reactions. This is because lighter isotopes are more reactive due to lower mass and bond energy (mass-dependent fractionation).[64] As the dissolution proceeded, efficient ion exchange between aqueous and solid phases yielded a reversal in the direction of the initial fractionation pattern ($\Delta^{18}O_P$ changed from negative to positive), consistent with past results[28,65] on O-isotopic fractionation between apatite mineral and dissolved phosphate. A small fractionation ($\Delta^{18}O_P \leq 1.3‰$) occurred during HANPs dissolution in three LMWOAs (Fig. 4), consistent with those (<3‰) on phosphate oxygen isotope fractionation during abiotic reactions.[25–28] These findings substantiate the fact that phosphate oxygen isotope fractionation is insignificant during apatite dissolution in abiotic systems.

Our $\Delta^{18}O_P$ data matched well with HANPs dissolution kinetics in both batch and column experiments: the $\Delta^{18}O_P$ increased from a negative value to zero at $t \approx 1$ h (Fig. 4a) and 2.5 PV (3.1 h) (Fig. 4b), respectively, in batch and column experiments at which time HANPs dissolution just reached equilibrium (Fig. 1 and 3). The increase in $\Delta^{18}O_P$ with HANPs dissolution in batch experiments is attributed predominately to enhanced exchange between $P^{16}O_4$ and $P^{18}O_4$ isotopes. The similar trend observed in column experiments, however, is due to preferential depletion of light isotopes in the reactant pool and the fact that ~100% HANPs were dissolved (Fig. 3a) based on isotope mass balance. Smaller isotope fractionation in batch (−0.3‰ to +1.1‰) than that in column (−1.3‰ to +1.1‰) experiments is a result of lower dissolution efficiency (≤30% *vs.* ~100%; Fig. 1 and 3), faster mass transfer rate (1 h *vs.* 3.1 h to reach equilibrium; Fig. 1 and 3), and greater ion ($P^{16}O_4$ and $P^{18}O_4$) exchange between HANPs and dissolved phosphates. Faster mass transfer rate results in less isotope fractionation, which is analogous to the mechanism that the more strongly bonded the isotope (corresponds to less mass transfer rate), the larger the fractionation effect.[64] For instance, Turner[66] reported that the C isotope enrichment factor during calcium carbonate precipitation was 1.4‰ under slow precipitation conditions (*i.e.*, low mass transfer rate), but this fractionation appeared to diminish during rapid precipitation conditions. The above interpretation is supported by the fact that during early states of dissolution, O-isotopic fractionation was significantly ($p = 0.017 < 0.05$; ANOVA analysis) smaller in batch than in column systems (−0.3‰ *vs.* −1.3‰; Fig. 4). Irrespective of the experimental system, the $\Delta^{18}O_P$ followed the order of acetic > oxalic > citric acid, which again can be interpreted by the differences in their mass transfer rate, *i.e.*, $R_{acetate} < R_{oxalate} < R_{citrate}$ (described above).

3.3.1. Rayleigh fractionation model. The Rayleigh model was used to quantify ^{18}O enrichment factor (ε_0) in dissolved phosphates. The linearized ^{18}O-enrichment of dissolved phosphate in column experiments indicates that the model well captured ^{18}O-enrichment (Fig. 5). The Rayleigh model was not used to fit the $\delta^{18}O_P$ data in batch experiments because of additional reactions (*e.g.*, phosphate sorption–desorption) that complicate the expected trend of isotope enrichment.[65] The ε_0 values of the slopes of regression lines in Fig. 5 fall within a narrow range of 0.37–1.35‰. The order of ε_0 values under three LMWOAs in column experiments was acetic > oxalic > citric acid (1.35‰ > 0.72‰ > 0.37‰; Fig. 5), consistent with the trends of their corresponding $\Delta^{18}O_P$ values (Fig. 4b). Enrichment in ^{18}O-phosphate has also been documented by Liang and Blake.[28] These findings verify the applicability of the Rayleigh model in describing O-isotopic fractionation for NPs during abiotic reactions. A negative correlation existed between ε_0 and R in different LMWOAs, highlighting that the dissolution rate during mineral dissolution (acid etching) is likely a potential indicator quantifying the magnitude of isotope fractionation.

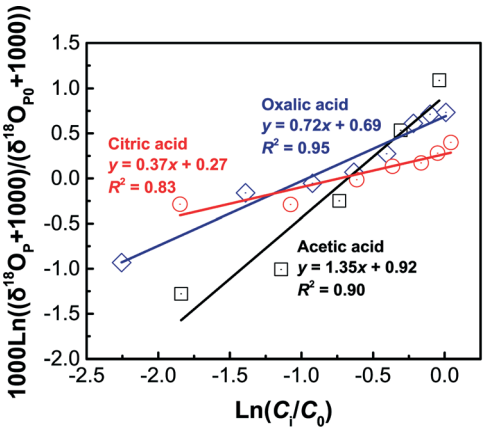

Fig. 5 Linearized ^{18}O-enrichment in column dissolution experiments under different LMWOAs (1 mM acetic acid, oxalic acid, and citric acid, respectively) at C_0 = 0.2 g L^{-1} according to the Rayleigh model.

4. Conclusions and environmental implications

Both batch and column experiments were conducted to unravel the dissolution kinetics of HANPs under different types of LMWOAs. Our results indicate that the dissolution of HANPs is dependent on the experimental system, solution pH, ligand type, and/or dissolution stage. Specifically, protons plays a dominant role in HANPs dissolution during early stages particularly for the column system, whereas organic ligands take over the dissolution during later stages in the batch system. The isotopically lighter phosphate ($P^{16}O_4$) was preferentially released during early stages of dissolution and dissolved phosphate became gradually $P^{18}O_4$-enriched with time. The O-isotopic evolution of dissolved phosphate under three LMWOAs can be well described by the Rayleigh fractionation model.

Our study provides several insights into dissolution kinetics and bioavailability of HANPs in plant–soil systems where they are being proposed as a P nanofertilizer. It is well-recognized that even though the total amount of P in soils greatly exceeds crop requirement, the plant-available P is

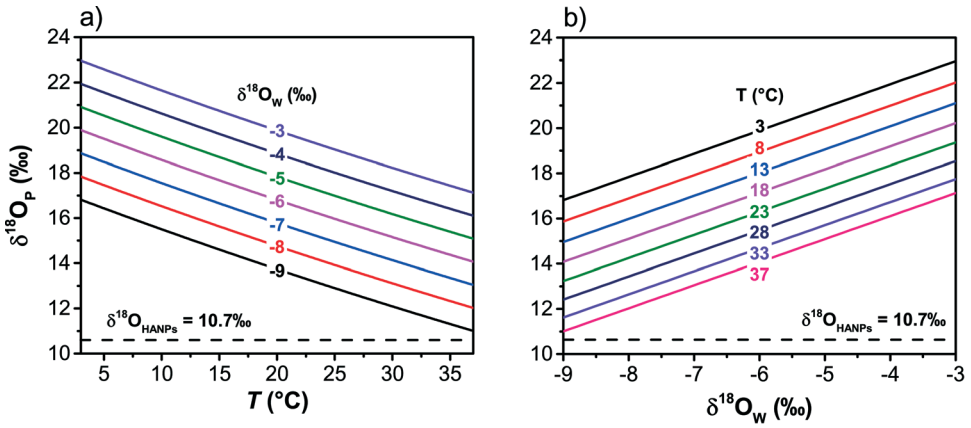

Fig. 6 Calculated equilibrium value of dissolved phosphate ($\delta^{18}O_P$) under a wide range of environmentally relevant temperatures (a; from 3 to 37 °C) and water oxygen isotopes ($\delta^{18}O_W$) (b; water oxygen isotope ratios, from −9‰ to −3‰) using the equation of Chang and Blake.[68] The dash line represents the $\delta^{18}O_{HANPs}$ value (10.7‰) of the bulk (starting) HANPs.

insufficient particularly in most acidic soils (pH <5.5) that occupy ~30% of the world's arable land.[67] Our data suggest that direct application of HANPs in these acidic soils is expected to provide bioavailable P (PO_4^{3-} ion) for crop growth in a timely fashion due to quick proton-promoted dissolution. The dissolution rate constant could be much higher in the rhizosphere where acetic, oxalic, and citric acids are present in large quantities and undergo both proton- and ligand-promoted dissolution of the HANPs. The dissolution of HANPs is greatest for citric followed by oxalic acids, and acetic acid is the least effective at releasing P. However, acetic acid appears to be the most efficient at furnishing P nutrient during the crop growing period attributed to its low HANPs dissolution rate, thereby providing P in an appreciable quantity for a long time (Fig. 3a and S11a†).

Over a wide range of environmentally relevant temperatures (3–37 °C) and $\delta^{18}O_W$ values (water oxygen isotope ratios, −9‰ to −3‰),[19,20,68] the $\delta^{18}O_P$ equilibrium value of dissolved phosphate ranges from 11.0‰ to 23.0‰ (Fig. 6), which is different from the $\delta^{18}O_{HANPs}$ value (10.7‰) of bulk HANPs with $\Delta^{18}O_P$ = 0.3–12.3‰. Consequently, the dissolved phosphates from HANPs dissolution are expected to cycle and attain equilibrium due to enzymatically catalyzed hydrolysis in agricultural soils. An important distinction to be made here is the original isotope composition *vs.* the equilibrium isotope composition. If the original isotope composition of HANPs (or corresponding dissolution products) is far from equilibrium (Fig. 6) under environmentally relevant conditions, identification of the source signature will be straightforward. Clearly, significant isotope excursion is needed in the systems at low temperatures (Fig. 6a) and high $\delta^{18}O_W$ values (Fig. 6b) to achieve isotope equilibrium. During isotope excursion to achieve equilibrium, several reactions may occur: dissolved phosphate could be sorbed or occluded in soils and thus could retain original or partially exchanged isotope signals for a longer time and allow identification of source(s). Even if soil P pools are transformed, the trend of isotope excursion may provide useful information that could help identify the pathway of this transformation.[29] Overall, given that the HANPs pool has distinct phosphate oxygen isotope signatures compared to soil P pools,[29] the O-isotope technique could be used to identify whether plant uptake of P comes from HANPs or from soils, and thus to evaluate the use efficiency of HANPs by plants in agricultural soils.

Acknowledgements

This research was funded by the U.S. Department of Agriculture (NIFA Awards 2013-67019-21373 and 2015-67020-23603). We appreciate Yimin Wang (College of Environment, Hohai University) for assisting the speciation calculation of LMWOAs.

References

1 B. S. Sekhon, *Nanotechnol., Sci. Appl.*, 2014, **7**, 31–53.
2 R. Liu and R. Lal, *Sci. Total Environ.*, 2015, **514**, 131–139.
3 D. Cordell, J. O. Drangert and S. White, *Glob. Environ. Change*, 2009, **19**, 292–305.
4 J. M. Hughes and J. F. Rakovan, *Elements*, 2015, **11**, 165–170.
5 R. Liu and R. Lal, *Sci. Rep.*, 2014, **4**, 5686–5691.
6 D. Montalvo, F. Degryse and M. J. McLaughlin, *Soil Sci. Soc. Am. J.*, 2015, **79**, 577–584.
7 E. Frossard, M. Brossard, M. J. Hedley and A. Metherell, in *Phosphorus Cycling in Terrestrial and Aquatic Ecosystems: A Global Perspective*, ed. H. Tiessen, SCOPE/John Wiley, 1995, pp. 107–137.
8 T. R. Fox and N. B. Comerford, *Soil Sci. Soc. Am. J.*, 1990, **54**, 1139–1144.
9 D. L. Jones, *Plant Soil*, 1998, **205**, 25–44.
10 P. Hinsinger, *Plant Soil*, 2001, **237**, 173–195.
11 G. Furrer and W. Stumm, *Geochim. Cosmochim. Acta*, 1986, **50**, 1847–1860.
12 B. Zinder, G. Furrer and W. Stumm, *Geochim. Cosmochim. Acta*, 1986, **50**, 1861–1869.

13 J. I. Drever and L. L. Stillings, *Colloids Surf., A*, 1997, **120**, 167–181.
14 A. Longinelli and S. Nuti, *Earth Planet. Sci. Lett.*, 1973, **19**, 373–376.
15 R. E. Barrick and W. J. Showers, *Science*, 1994, **265**, 222–224.
16 R. E. Blake, S. J. Chang and A. Lepland, *Nature*, 2010, **464**, 1029–1032.
17 R. E. Blake, J. R. O'Neil and G. A. Garcia, *Geochim. Cosmochim. Acta*, 1997, **61**, 4411–4422.
18 A. Paytan, Y. Kolodny, A. Neori and B. Luz, *Global Biogeochem. Cycles*, 2002, **16**, 13.
19 D. C. Gooddy, D. J. Lapworth, S. A. Bennett, T. H. E. Heaton, P. J. Williams and W. J. Surridge, *Water Res.*, 2016, **88**, 623–633.
20 D. C. Gooddy, D. J. Lapworth, M. J. Ascott, S. A. Bennett, T. H. E. Heaton and W. J. Surridge, *Environ. Sci. Technol.*, 2015, **49**, 9020–9028.
21 R. E. Blake, J. R. O'Neil and A. V. Surkow, *Am. J. Sci.*, 2005, **305**, 596–620.
22 C. Lecuyer, P. Grandjean and S. M. F. Sheppard, *Geochim. Cosmochim. Acta*, 1999, **63**, 855–862.
23 J. R. O'Neil, T. W. Vennemann and W. F. McKenzie, *Geochim. Cosmochim. Acta*, 2003, **67**, 3135–3144.
24 D. P. Jaisi and R. E. Blake, *Adv. Agron.*, 2014, **125**, 1–53.
25 D. P. Jaisi, R. E. Blake and R. K. Kukkadapu, *Geochim. Cosmochim. Acta*, 2010, **74**, 1309–1319.
26 D. P. Jaisi, *J. Contam. Hydrol.*, 2013, **154**, 10–19.
27 D. Wang, Y. Jin and D. P. Jaisi, *J. Contam. Hydrol.*, 2015, **182**, 194–209.
28 Y. Liang and R. E. Blake, *Chem. Geol.*, 2007, **238**, 121–133.
29 S. R. Joshi, X. Li and D. P. Jaisi, *Soil Sci. Soc. Am. J.*, 2016, **80**, 69–78.
30 F. Tamburini, V. Pfahler, C. von Sperber, E. Frossard and S. M. Bernasconi, *Soil Sci. Soc. Am. J.*, 2013, **78**, 38–46.
31 D. Wang, S. A. Bradford, R. W. Harvey, B. Gao, L. Cang and D. M. Zhou, *Environ. Sci. Technol.*, 2012, **46**, 2738–2745.
32 D. Wang, Y. Jin and D. P. Jaisi, *Environ. Sci. Technol.*, 2015, **49**, 8461–8470.
33 S. A. Welch, A. E. Taunton and J. F. Banfield, *Geomicrobiol. J.*, 2002, **19**, 343–367.
34 A. I. Schafer, A. G. Fane and T. D. Waite, *Desalination*, 2000, **131**, 215–224.
35 J. Liu and R. H. Hurt, *Environ. Sci. Technol.*, 2010, **44**, 2169–2175.
36 T. Harter, S. Wagner and E. R. Atwill, *Environ. Sci. Technol.*, 2000, **34**, 62–70.
37 B. Nowack, J. F. Ranville, S. Diamond, J. A. Gallego-Urrea, C. Metcalfe, J. Rose, N. Horne, A. A. Koelmans and S. J. Klaine, *Environ. Toxicol. Chem.*, 2012, **31**, 50–59.
38 W. X. Zhang, *J. Nanopart. Res.*, 2003, **5**, 323–332.
39 J. Murphy and J. P. Riley, *Anal. Chim. Acta*, 1962, **27**, 31–36.
40 D. Wang, L. Chu, M. Paradelo, W. J. G. M. Peijnenburg, Y. Wang and D. Zhou, *J. Colloid Interface Sci.*, 2011, **360**, 398–407.
41 F. Tamburini, S. M. Bernasconi, A. Angert, T. Weiner and E. Frossard, *Eur. J. Soil Sci.*, 2010, **61**, 1025–1032.
42 M. W. Guidry and F. T. Mackenzie, *Geochim. Cosmochim. Acta*, 2003, **67**, 2949–2963.
43 C. Chairat, J. Schott, E. H. Oelkers, J. E. Lartigue and N. Harouiya, *Geochim. Cosmochim. Acta*, 2007, **71**, 5901–5912.
44 K. W. Ulrich, A. Singh, E. J. Schofield, J. R. Bargar, H. Veeramani, J. O. Sharp, R. Bernier-Latmani and D. E. Giammar, *Environ. Sci. Technol.*, 2008, **42**, 5600–5606.
45 S. V. Dorozhkin, *Prog. Cryst. Growth Charact. Mater.*, 2002, **44**, 45–61.
46 J. L. Fox, W. I. Higuchi, M. B. Fawzi and M. S. Wu, *J. Colloid Interface Sci.*, 1978, **67**, 313–320.
47 M. B. Fawzi, J. L. Fox, M. G. Dedhiya, W. I. Higuchi and J. J. Hefferren, *J. Colloid Interface Sci.*, 1978, **67**, 304–311.
48 W. Dansgaard, *Tellus*, 1964, **16**, 436–468.
49 K. Kpomblekou and M. A. Tabatabai, *Agric., Ecosyst. Environ.*, 2003, **100**, 275–284.
50 E. Valsami-Jones, K. V. Ragnarsdottir, A. Putnis, D. Bosbach, A. J. Kemp and G. Cressey, *Chem. Geol.*, 1998, **151**, 215–233.
51 L. Wu, W. Forsling and P. W. Schindler, *J. Colloid Interface Sci.*, 1991, **147**, 178–185.
52 W. Stumm, *Colloids Surf., A*, 1997, **130**, 143–166.
53 K. W. Goyne, S. L. Brantley and J. Chorover, *Chem. Geol.*, 2006, **234**, 28–45.
54 J. I. Drever, *Geochim. Cosmochim. Acta*, 1994, **58**, 2325–2332.
55 M. R. T. Filgueiras, D. Mkhonto and N. H. de Leeuw, *J. Cryst. Growth*, 2006, **294**, 60–68.
56 C. Christophe, T. Marie-Pierre, F. K. Pascale, U. Stephane, P. Marie-Claire, T. Zornitza and K. Antoine, *Geochim. Cosmochim. Acta*, 2013, **106**, 287–306.
57 J. Liu, D. A. Sonshine, S. Shervani and R. H. Hurt, *ACS Nano*, 2010, **4**, 6903–6913.
58 T. S. Peretyazhko, Q. Zhang and V. L. Colvin, *Environ. Sci. Technol.*, 2014, **48**, 11954–11961.
59 S. Aramrak, M. Flury, J. B. Harsh, R. L. Zollars and H. P. Davis, *Langmuir*, 2013, **29**, 5770–5780.
60 M. B. Seymour, G. Chen, C. Su and Y. Li, *Environ. Sci. Technol.*, 2013, **47**, 8391–8398.
61 C. Kendall, in *Isotope Tracers in Catchment Hydrology*, ed. C. Kendall and J. J. McDonnell, Elsevier Science, Amsterdam, 1998, pp. 519–576.
62 J. R. O'Neil, R. N. Clayton and T. K. Mayeda, *J. Chem. Phys.*, 1969, **51**, 5547–5558.
63 A. V. Turchyn, B. Volker, T. W. Lyons, G. S. Engel, N. Balci, D. P. Schrag and B. Brunner, *Geochim. Cosmochim. Acta*, 2010, **74**, 2011–2024.
64 J. F. Duncan and G. B. Cook, *Isotopes in Chemistry*, Clarendon Press, Oxford, 1968, p. 273.
65 D. P. Jaisi, R. K. Kukkadapu, L. M. Stout, T. Varga and R. E. Blake, *Environ. Sci. Technol.*, 2011, **45**, 6254–6261.
66 J. V. Turner, *Geochim. Cosmochim. Acta*, 1982, **46**, 1183–1191.
67 H. R. von Uexkull and E. Mutert, *Plant Soil*, 1995, **171**, 1–15.
68 S. J. Chang and R. E. Blake, *Geochim. Cosmochim. Acta*, 2015, **150**, 314–329.